scientific reports

Check for updates

OPEN

Towards bright gamma-ray flash generation from tailored target irradiated by multi-petawatt laser

Prokopis Hadjisolomou[1]✉, Tae Moon Jeong[1] & Sergei V. Bulanov[1,2]

One of the remarkable phenomena in the laser-matter interaction is the extremely efficient energy transfer to γ-photons, that appears as a collimated γ-ray beam. For interactions of realistic laser pulses with matter, existence of an amplified spontaneous emission pedestal plays a crucial role, since it hits the target prior to the main pulse arrival, leading to a cloud of preplasma and drilling a narrow channel inside the target. These effects significantly alter the process of γ-photon generation. Here, we study this process by importing the outcome of magnetohydrodynamic simulations of the pedestal-target interaction into particle-in-cell simulations for describing the γ-photon generation. It is seen that target tailoring prior the laser-target interaction plays an important positive role, enhancing the efficiency of laser pulse coupling with the target, and generating high energy electron-positron pairs. It is expected that such a γ-photon source will be actively used in various applications in nuclear photonics, material science and astrophysical processes modelling.

Since the invention of the Chirped Pulse Amplification technique[1], development of multi-petawatt (multi-PW) laser systems is envisioned worldwide. The lasers with the 10 PW peak power are coming in operation at the ELI-Beamlines[2], Czech Republic, with an energy of 1.5 kJ, and at the ELI-NP[3], Romania, with a pulse duration of 25 fs but approximately five times lower energy compared to ELI-Beamlines. The ELI-ALPS, Hungary, aims at constructing an ultrashort 17 fs laser of 2 PW[4]. The laser combining pulses shorter than 20 fs in the 10 PW level is developed in Apollon facility[5], in France. By focusing a multi-PW laser down to a micrometer-wide spot[6,7], intensities exceeding 10^{27} Wm^{-2} can be achieved, where this threshold has been recently surpassed by the 4 PW CoReLS laser[7], South Korea.

A typical high power laser consists of an ultrashort main pulse, preceded by a lower amplitude amplified spontaneous emission (ASE) pedestal extending in the nanosecond scale[8]. The laser contrast is defined as the ratio of the main pulse amplitude to the ASE pedestal amplitude. Usually, in high power laser systems the contrast is increased through complex and/or expensive additions, such as Optical Parametric Chirped Pulse Amplification[9] and plasma mirrors[8,10].

The importance of a finite contrast for laser-matter interactions is highlighted both experimentally[11–14] and theoretically[12,13,15–17]. By assuming an initially steep density gradient (flat-foil, or simply foil) target, in the aforementioned literature it is agreed that the ASE pedestal modifies the initial density profile at an extent proportional to its amplitude and duration. A relatively thick (micrometer range) foil is curved in the vicinity of the laser focal spot, where a gradually increasing density profile appears in the target front region. On the other hand, if the target is thin enough then the ASE pedestal drills the target resulting in no interaction when the main pulse arrives. As a result, the preplasma strongly affects the energy spectra and directionality of particles emitted due to the laser-target interaction. However, since computational studies of the interaction typically involve particle-in-cell (PIC) simulations which cannot be applied to model the nanosecond long duration required by the ASE pedestal, usually a foil target is assumed, acknowledging only the effect of the main pulse on target.

A plethora of exotic target geometries has been already considered for laser-matter interaction experiments. Among numerous examples, we mention proton-rich micro-dots[18], cylindircal micro-lenses[19,20], hollow micro-spheres[21], micro-coils[22] and wavelength-scale holed targets[23,24]. All of the aforementioned target designs require explicit microfabrication techniques, while they add further complexity to a laser-target experiment since they require additional efforts on positioning and alignment of the target. However, it was noticed that the use of tailored targets is favorable for the laser-target interaction and their use is widely employed.

[1]ELI Beamlines Centre, Institute of Physics, Czech Academy of Sciences, Za Radnicí 835, 25241 Dolní Břežany, Czech Republic. [2]National Institutes for Quantum and Radiological Science and Technology (QST), Kansai Photon Science Institute, 8-1-7 Umemidai, Kizugawa Kyoto 619-0215, Japan. ✉email: prokopis.hadjisolomou@eli-beams.eu

Apart of target tailoring methods outside the interaction chamber, it is also possible to manipulate the electron density profile by means of a secondary, long pulse duration, lower power laser[25]. Temporal control of the secondary laser[26] can provide the required electron density distributions. This scheme is known as 'laser heater' and has been successfully implemented on improving the properties of laser driven particle beams[27,28]. Notably, manipulating the target density with a laser heater resulted in record energy values of particles accelerated by optical means[29].

At the ultrahigh intensity limit, the theory foresees that the multi-PW lasers interacting with matter will provide not only energetic charged particles (electrons (e^-), protons (p^+), heavy ions (i^+)) but also a plethora of high energy γ-photons and electron-positron (e^-- e^+) pairs. Once an electron (or positron) collides with the incident field it is scattered, resulting in alteration of its momentum and a γ-photon is emitted, in a process known as multiphoton Compton scattering. In the present work, we focus on γ-photons produced via the multiphoton Compton scattering dominating at ultrahigh intensities[30–33], produced within a time approximately equal to to the laser pulse duration. Notably, at lower intensities ($< 10^{27}$ Wm^{-2}) and significantly thick targets γ-photons can be also produced via Bremsstrahlung emission[34,35], where the present target geometry limits Bremsstrahlung contribution. Since 10 PW lases have just very recently became operational and have not yet been used for experiments[36], previous high-power laser experiments reporting γ-photon detection[37] could not be based on emission from Compton scattering, but on Bremsstrahlung emission instead. The γ-photon production then makes possible the production of e^-- e^+ pairs via the multiphoton Breit-Wheeler process[38], where a high energy γ-photon interacts with multiple laser photons. The laser to γ-photon energy conversion efficiency is defined as

$$\kappa_\gamma = \frac{\int_{\mathcal{E}_{min}}^{\mathcal{E}_{max}} \mathcal{E}_\gamma \left(dN_\gamma / d\mathcal{E}_\gamma\right) d\mathcal{E}_\gamma}{\mathcal{E}_l}, \tag{1}$$

where $\mathcal{E}_{min}$ is the minimum γ-photon energy, $\mathcal{E}_{max}$ is the maximum γ-photon energy, $\mathcal{E}_\gamma$ is the γ-photon energy, $dN_\gamma / d\mathcal{E}_\gamma$ is the number of γ-photons within an energy interval of $d\mathcal{E}_\gamma$ and $\mathcal{E}_l$ is the laser energy prior the interaction of the laser pulse with the target. Maximising κ_γ is required in photonuclear physics[39,40], for study of high energy density physics in materials science[41] and studies of astrophysical processes[42–45].

The recently available multi-PW lasers in combination with the broad application range of the γ-photons, draw the interest of several research groups, suggesting various methods to maximise κ_γ. An early suggestion is based on the reflected part of the laser pulse incident on an overdense target[46–48]. However, loss of significant laser energy towards the reflection region suggested the use of two counter-propagating pulses[49–52], later extending the scheme to multiple colliding pulses[53,54]. Apart from the all-optical approach, other groups suggested microfabricating sophisticated target schemes[55,56] or even combining a laser with either optically[57] or externally accelerated electrons[58]. Moreover, it was shown that by adding a chosen preplasma on the target front, κ_γ can also be increased[32,59].

In the present work, we investigate through PIC simulations bonded with the results from MHD simulations the interaction of multi-petawatt lasers with tailored targets. Our results indicate high κ_γ values for properly chosen target material. Moreover, tailoring of the targets plays a positive effect on increasing κ_γ. For the 10 PW case, κ_γ approaches 30 %. In addition, we exhibit intensification of the initial laser by an order of magnitude, reaching intensities high enough for $e^- - e^+$ pairs to be generated through the Breit-Wheeler process.

Hybrid magnetohydrodynamic and particle-in-cell simulations

In reference[60] it has been demonstrated through magnetohydrodynamic (MHD) simulations that a unique microfabrication of the foil target is achieved by a ASE pedestal corresponding to multi-PW lasers. The radial symmetry of the results allows their expansion on a $(\hat{\boldsymbol{x}}, \hat{\boldsymbol{y}}, \hat{\boldsymbol{z}})$ grid, where the laser propagation axis is set along $\hat{\boldsymbol{x}}$. Therefore one can obtain the three-dimensional (3D) electron number density distribution. The results of the MHD simulations are then used as initial conditions in PIC simulations, in a hybrid modelling scheme that reveals the physical processes governing the complete interaction of the main laser pulse with the newly formed density distribution.

The ASE pedestal sets a 60 ps duration region with intensity starting at 10^{19} Wm^{-2}, dropping exponentially to 10^{14} Wm^{-2}, and then continues with a constant intensity for 940 ps, as shown in Fig. 1B. The laser intensity spatial profile is represented by a Gaussian of 2.2 μm full-width-at-half-maximum, while its intensity is comparable with what was considered as cutting-edge laser main pulse intensity a few decades ago[25]. From reference[60] we choose a set of elements with approximately equally increasing electron number density, n_e, namely lithium (Li, $n_e \approx 1.39\times10^{29}$ m^{-3}), sodium (Na, $n_e \approx 2.79\times10^{29}$ m^{-3}), beryllium (Be, $n_e \approx 4.95\times10^{29}$ m^{-3}), carbon (C, $n_e \approx 6.02\times10^{29}$ m^{-3}), and aluminium (Al, $n_e \approx 7.83\times10^{29}$ m^{-3}).

The MHD simulation outcome for a lithium foil is shown in Fig. 1A, where lithium having the lowest density among all solids at room temperature it is affected the strongest. In agreement with previous works[16,32], a preplasma distribution is generated in the target front region, although with a large exponential coefficient for the electron number density gradient of 3.1×10^5 m^{-1}, shown by the red lineout in Fig. 1A, along the laser propagation axis. Notably, the preplasma exceeding the critical density, n_{cr}, extends for only 1 μm in the target front region.

The sizeable target (12 μm diameter and 10 μm thickness) ensures neither target curvature on the target rear, nor complete drilling and destruction of the target[16,17]. In addition to the preplasma formation, a conical-like cavity is generated within the target volume, with walls several times denser than the background. For lithium, the cavity has a depth of 4 μm and a base diameter of 6 μm. The Gaussian ASE pedestal profile allows stronger target deformation in the centre, where the cavity profile exhibits two off-centre symmetric vertexes (where the derivative of the curvature is zero). This unique tailored target is achievable with finite contrast lasers currently

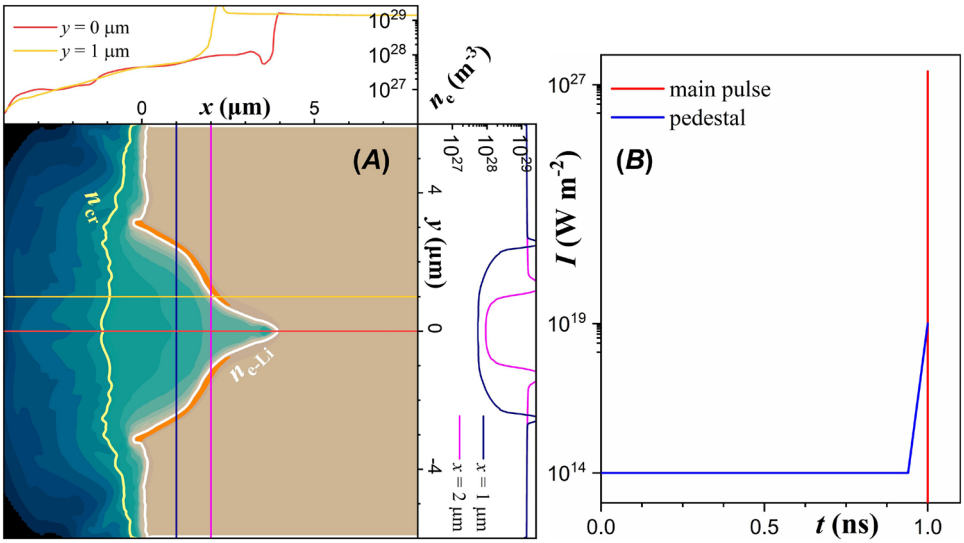

Figure 1. (**A**) Electron number density as given by MHD simulations (data taken from reference[60]), following irradiation of a lithium foil. The yellow contour line is at the critical density and the white contour line is at the lithium solid electron density. The orange saturated contour is overcritical for laser intensities above 10^{27} Wm^{-2}. (**B**) The ASE pedestal profile used in reference[60] (blue line) compared with the 10 PW main laser pulse profile presently employed (red line).

available, revealing a preplasma regime which to the best of our knowledge has never been considered in PIC simulations.

The PIC code used is the relativistic quantum electrodynamic EPOCH code[61], compiled with the Higuera-Cary[62] (to more accurately resolve electron trajectories), Bremsstrahlung and Photons[63] preprocessor directives enabled. The simulations are performed in the 3D version of the code, where the laser pulse and target characteristics match those of the MHD simulations, with main pulse focused intensity ranging from 2.8×10^{26} Wm^{-2} to 2.8×10^{27} Wm^{-2}. The corresponding energy is set from 20 J to 200 J, while a pulse duration of 17 fs[4,7] corresponds to lasers of 1 PW to 10 PW power. The central laser wavelength is set to 815 nm, typical for titanium-sapphire lasers. The laser focal spot is set at the centre of the front surface of a foil target.

The MHD density array, after interpolation to a $10\times40\times40$ nm cell size grid, is centred and expanded in a cubic PIC volume, extending from -15.36 μm to 15.36 μm in all three directions. The cell dimensions are chosen small enough to accurately resolve the relativistic skin depth, while 8 macro-electrons and 8 macro-ions are assigned to each cell. The simulation ran for 110 fs, enough for κ_γ to saturate and at the same time neither field energy nor energetic electrons escape the simulation box from the open boundaries. The laser is focusing at a simulation time of 65 fs, which is set as 0 fs for the laser-target interaction. The simulations run on the ECLIPSE cluster, ELI-Beamlines, on 1024 cores.

Cavity propagation and intensity enhancement

In the present work, the default target referral is a tailored lithium target and the default laser power is 10 PW, except where it is stated otherwise. The conical-like cavity presently used resembles laser-target interaction geometries on which a cone is purposely fabricated at the target, aiming at novel fast-ignition schemes[64,65], increasing laser induced γ-photon production[66], enhancing laser field intensity[67], and efficient proton acceleration[68,69]. The cavity formation in the radiation reaction regime is related to fast-ion ignition[70] and ion acceleration[71]. In particular, the radiation friction effects result in suppressing the laser pulse filamentation.

In typical laser-solid interaction experiments, an oblique incidence angle is required to avoid laser back-reflection that could lead to laser damage and/or to icnrease the laser-target coupling. A normal laser incidence can be considered if the laser system is equipped with a series of Faraday isolators. When the theoretical predictions of our work are adjusted to a particular laser system, further simulations addressing the effect of a non-normal incidence angle should be performed, along with the other parameters of the specific laser beam.

The interaction of an ultra-intense laser pulse with a foil target results in electron acceleration by the electromagnetic field[72]. Since the frequency of the electromagnetic force is double the laser frequency, twice in every cycle a population of electrons is accelerated into the plasma, and a hole starts evolving on the target. Electrons absorb a significant portion of the laser energy, where their energy spectrum has an exponentially decaying profile with a decay temperature comparable to the ponderomotive potential. As the laser penetrates the target within the cavity region, the laser electric field drives plasma electrons on the edge of the hole and the absorption efficiency increases. In undercritical density regions, laser energy transfer to hot electrons is attributed not only to the oscillating ponderomotive force, but also to Raman instability. Moreover, the case of pulse evolution within relativistic channels have been demonstrated[73]. In our simulations, when the laser field peaks, high electron momentum values exist within an angle of approximately 45^o with respect to the laser propagation axis. As the emission direction of high energy γ-photons is approximately that of the electrons, the γ-photon distribution

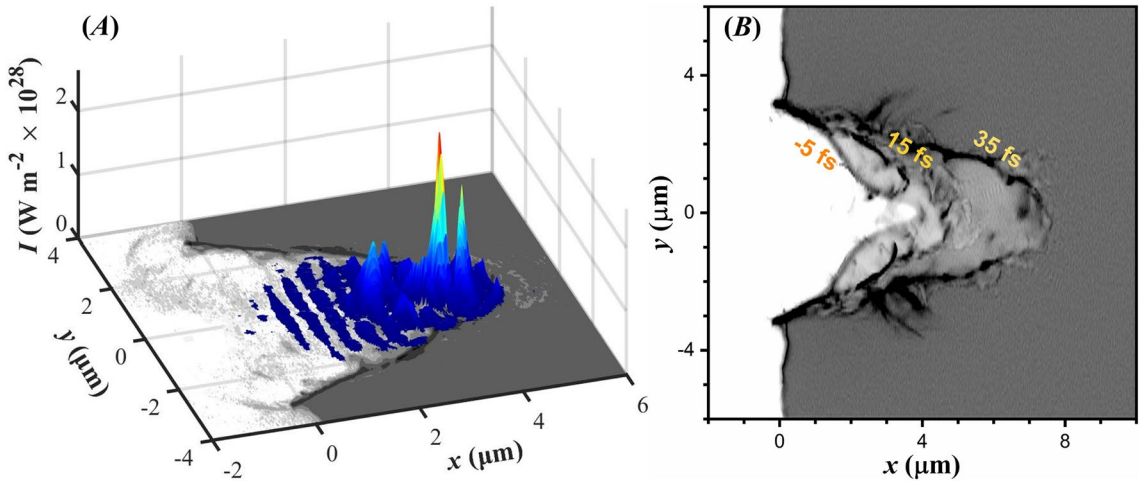

Figure 2. (**A**) Laser intensity (color surface plot) overlaid on the lithium electron number density (grayscale image) at 15 fs, when an intensity of 2.6×10^{28} Wm^{-2} is reached. (**B**) Overlay of three successive electron number density distributions, with a time step of 20 fs. The first layer is at −5 fs, when the main pulse is within the cavity. The overlay of the three layers reveals the temporal dynamics of the cavity formation within the target.

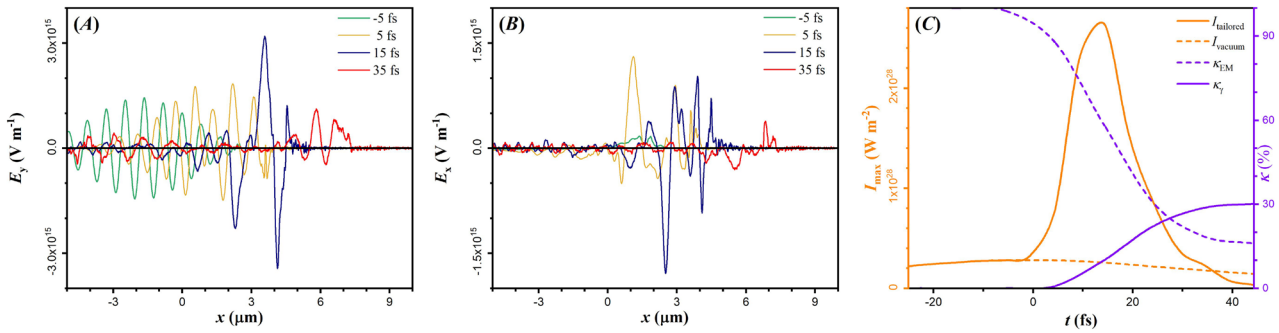

Figure 3. (**A**) Line-out of E_y, and (**B**) line-out of E_x along the laser propagation axis at various times, as noted on the legend. Note that the laser is linearly polarized, along $\hat{\boldsymbol{y}}$. (**C**) The left axis shows the maximum field intensity as a function of simulation time; the black dashed baseline denotes the field intensity expected in the focal spot, without the target. The right axis shows with the dashed purple line the amount of laser energy transferred to all target particles, while the solid purple line shows the percentage of the remaining laser field energy, κ_γ, as a function of time.

is unavoidably related to that of electrons, in connection to the findings regarding the γ-ray flash divergence, discussed later in the manuscript.

Since in our case the relativistic critical density is above lithium electron number density, one might expect the cavity formation to have no effect on focusing the laser field, due to dominance of relativistic self-focusing[74] of the laser field in the underdense solid. However, as seen by the spikes in the density line-out profiles in Fig. 1A, a thin, overdense layer is formed on the cavity walls. As a result, the laser field can penetrate only within the skin-depth of the walls, and reflected towards the cavity depth.

The reflected fields then interfere, rapidly increasing the field intensity. Note that the laser focal spot is at the base of the cone, meaning that in vacuum the laser would be defocusing if the cavity did not exist. In addition, the cavity volume is filled with a low electron density, that also aids focusing due to weak relativistic self-focusing; although to a lesser extent than the cavity focusing, as its electron density increases exponentially.

Once the laser is intensified in the cavity, its intensity surpasses that expected in the focal spot. As a result, the thin overdense electron distribution becomes undercritical, and the laser breaks into the target volume[75], where the lithium density had an initially constant value. In addition, field reflection by the cavity walls results in caustics, instantaneously increasing the field intensity. These effects are seen in Fig. 2A, where the laser intensity is shown when reaching its maximum value of 2.6×10^{28} Wm^{-2}, an order of magnitude higher than the intensity expected at the focal spot. The electron number density is over-plotted on the figure, visualizing the spatial location of the laser field with respect to the cavity. The highest intensity is recorded at 15 fs after the laser field reaches the focal spot.

Figure 3A and B show line-outs (along laser propagation axis) of the transverse and longitudinal components of the electric field ($\mathbf{E_y}$ and $\mathbf{E_x}$ respectively) at successive times. When the laser field arrives at the cavity (at −5 fs),

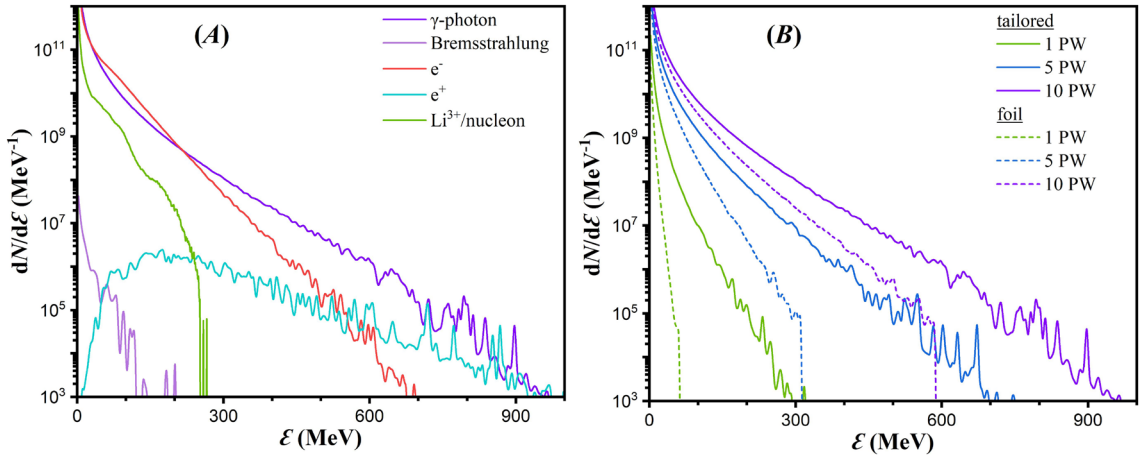

Figure 4. (**A**) Energy spectra after a 10 PW laser interacts with a tailored lithium target. (**B**) Energy spectra of γ-photons after interaction of the main laser pulse (of power as indicated on the figure legend) with a lithium target, as noted on the legend. The solid lines correspond to tailored targets, and the dashed lines to foil targets.

$\mathbf{E_x}$ is practically absent. However, reflection of the laser field on the cavity walls allows not only interference of $\mathbf{E_y}$ but also generation of $\mathbf{E_x}$, where the magnitude of the two field components is comparable since $E_y \approx 2E_x$ for times after 0 fs. Existence of $\mathbf{E_x}$ ceases only when both field components dissipate, near the end of the simulation.

Penetration of the laser field in the target at successive times is shown in Fig. 2B, by overlaying three electron density contours. The colour magnitude serves purely for visualization purposes, since appropriate contrast is applied to the figure to reveal the cavity propagation. Although the laser can penetrate the relativistically under-critical target, its propagation is further assisted by $\mathbf{E_x}$, which further drills the target along its propagation axis.

As a result, the laser pulse can maintain high intensities until the end of the simulation, although dissipating due to energy transfer to electrons and γ-photons. This can be seen in Fig. 3C, where the left axis plots the laser peak intensity as a function of time. For comparison, the orange dashed line is the intensity in the focal spot in vacuum. At -5 fs the laser field is in a region of extremely low electron density, also in the vicinity of the focal spot region. Therefore, the peak intensity coincides with the expected peak intensity in vacuum. Beyond that time, up to 15 fs, the intensity is increasing. At that time interval most of the field energy is transferred to the rest of particles (γ-photons, electrons, positrons, ions), shown by the dashed purple line in Fig. 3C.

Laser energy conversion to particle energy continues up to 35 fs, where the peak intensity drops since no significant laser energy remains within the propagating cavity. The laser field energy saturates at 15 % of its initial value, due to laser back-reflection. The κ_γ, shown by the solid purple line, exhibits a sigmoidal behaviour[76] with changing curvature at the time the laser intensity is maximised, saturating at 30 %. Remarkably, conversion of approximately one third of the laser energy to γ-photons with the currently available technology, is of interest for worldwide laser facilities.

Gamma-ray flash scaling with power and target material

The aforementioned laser-target interaction leads to a plethora of energetic electrons in the GeV-scale, which in turn result in ion acceleration with energies per nucleon of approximately 300 MeV as seen in Fig. 4A. We should clarify that optimizing ion acceleration is not among the goals of the present work, hence the thick target chosen. By considering that for optimal laser coupling to electrons[12,77,78] the condition

$$a_0 = \pi \frac{n_e}{n_{cr}} \frac{l}{\lambda} \tag{2}$$

must be satisfied (where a_0 is the dimensionless amplitude and l is the penetration depth per wavelength), it can be calculated that the intensity ranges shown in Fig. 3C correspond to $1\ \mu\text{m} < l < 3\ \mu\text{m}$. Since the temporal pulse length is 6λ, it is estimated that a $10\ \mu$m thick target is required for the laser pulse to efficiently transfer its energy to the target.

In the present work we consider γ-photons produced by either Bremsstrahlung radiation or multiphoton Compton scattering. However, the micrometer-thick, low atomic number target is unsuitable for Bremsstrahlung emission, although the emission continues for a significantly longer time than the pulse duration. In addition, the stochastic dynamics of electrons in the solid target results in a non-directional Bremsstrahlung emission, making γ-photons from Compton scattering dominate the γ-photon signal during ultraintense laser-matter experiments. The Compton γ-photon spectrum is comparable to the electron spectrum, as seen in Fig. 4A, with a temperature of 55 MeV for γ-photons of $>$ 200 MeV energy. For comparison, the Bremsstrahlung spectrum at the end of the simulation is also shown, which is several orders of magnitude lower than the Compton spectrum. However, its contribution can only increase the cumulative γ-photon energy, with a κ_γ of 30 % only from Compton scattering contribution. Hence, the default γ-photon referral is Compton scattering. The energy spectrum evolution, being a dynamic process, does not violate the fact that the parent electron responsible for a γ-photon is of higher energy than the resulting γ-photon. A temporal evolution of the electron spectrum (not shown) demonstrates

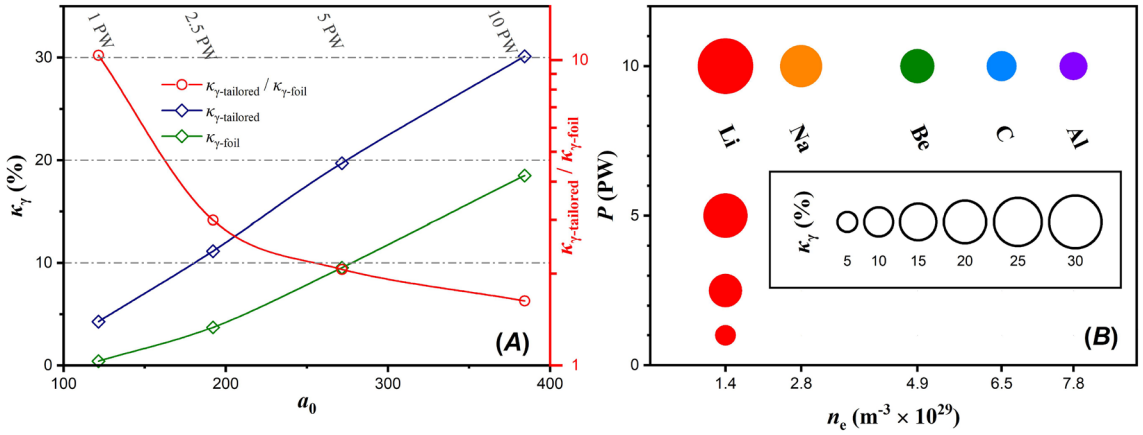

Figure 5. (**A**) The left axis shows κ_γ as a function of a_0, for tailored (blue) and foil (green) lithium targets. The right axis shows the ratio of the two aforementioned cases. (**B**) κ_γ as a function of laser power, for various tailored target materials. The κ_γ value is proportional to the circle area.

an increase of the maximum electron energy at the initial stages of the simulation, which then decreases due to both emission of γ-photons and energy transfer to ions.

At high intensity laser-matter interactions, generation of e^-- e^+ pairs is possible through the multiphoton Breit-Wheeler process. Although e^-- e^+ pair generation is not expected to be observed for a 10 PW laser (corresponding to intensities of 2.8×10^{27} Wm^{-2}), we demonstrate that the one order of magnitude intensity enhancement due to the tailored target makes multiphoton Breit-Wheeler e^-- e^+ pair production feasible. The positron spectrum is shown in Fig. 4A, spanning up to the maximum γ-photon energy with a Maxwell-Juttner distribution of 80 MeV temperature, where 4×10^8 pairs are recorded. Additional e^-- e^+ pairs can be produced by laser interacting with heavy targets either through electroproduction[79], or through the Bethe-Heitler process[57,80], both seen experimentally by lower power lasers implementing high-Z targets (where Z is the atomic number of the target material). However, by considering that the cross-section of the latter processes scales as Z^2 (in our results we implement lithium targets with $Z^2 = 9$, compared to 6724 for lead typically used in experiments), in combination with the micrometre-thick targets assumed in our work versus the massive targets used for experimental observation of those processes, their contribution to the overall positron population is reduced.

The preformed cavity importance on κ_γ optimization and γ-photon maximum energy increase is seen in Fig. 4B by comparing the solid lines (tailored target) with the dashed lines (foil target) for various laser powers. In all cases, the cavity formation significantly amplifies the γ-photon spectrum, where the exponential behaviour still persists but with decreasing temperature for decreased power. The quantitative results for κ_γ as a function of a_0 are shown in Fig. 5A, where the blue line corresponds to tailored targets and the green to foil targets. The figure reveals an almost linear dependency of κ_γ to a_0 (or to the laser power) within the range of interest.

The right axis of Fig. 5A shows the ratio of κ_γ from tailored to that of foil lithium targets as a function of a_0. Notably, for a 10 PW laser the ratio is 1.5, but rising to 10 for a 1 PW laser. This result is related to the relativistic transparency of lithium for the 10 PW case, where even in the case of no cavity formation the laser pulse is still efficiently penetrating the target. On the other hand, the 1 PW case relies on intensity enhancement within the cavity to reach the relativistic transparency threshold, whilst the foil target strongly reflects the laser pulse with little-to-no conversion to γ-photons. Therefore, even single-PW lasers can be used to efficiently create a γ-ray flash in the laboratory.

In connection to the high κ_γ for lithium targets, the results for denser materials are shown in the columns of Fig. 5B, where the rows correspond to varying laser power. Study of the dependency of κ_γ on the target material is performed only for the 10 PW case, since in all lower powers it follows a similar trend. For the materials considered, it is found that κ_γ is inversely proportional to n_e. By increasing the target density, two effects result in reduced κ_γ. Firstly, the cavity formation is less prominent in a denser material, resulting in lower intensity amplification. Secondly, the target electron number density shifts away from the relativistic critical density and the laser field can no longer be efficiently coupled to the target electrons. Notably, materials commonly used in experiments have an electron density of a few times higher than that of lithium (e.g. approximately five times for aluminium). As a result, if aluminium is used in a 10 PW γ-ray flash experiment, κ_γ will be significantly suppressed. The main drawback of lithium is its high chemical reactivity in air. Fortunately, a thin (sub-micron) polymer coating does not significantly alter the laser interaction with the target since it is drilled by the laser ASE pedestal before the main pulse arrives. In addition, the laser-target interaction takes place in vacuum.

Gamma-ray flash parameters

So far, we have quantitatively described the laser generated γ-ray flash at various laser powers and for various target materials, demonstrating that κ_γ can reach significantly high values if a cavity-like structure is tailored on the target. Here, the absolute value of κ_γ is obtained by integrating γ-photons emitted in a 4π solid angle. It has been previously demonstrated for a linearly polarized laser that either by employing specific targets (cylindrical channel[81,82] or tightly focused lasers[83]), γ-photon emission is stronger in two directions along the polarization

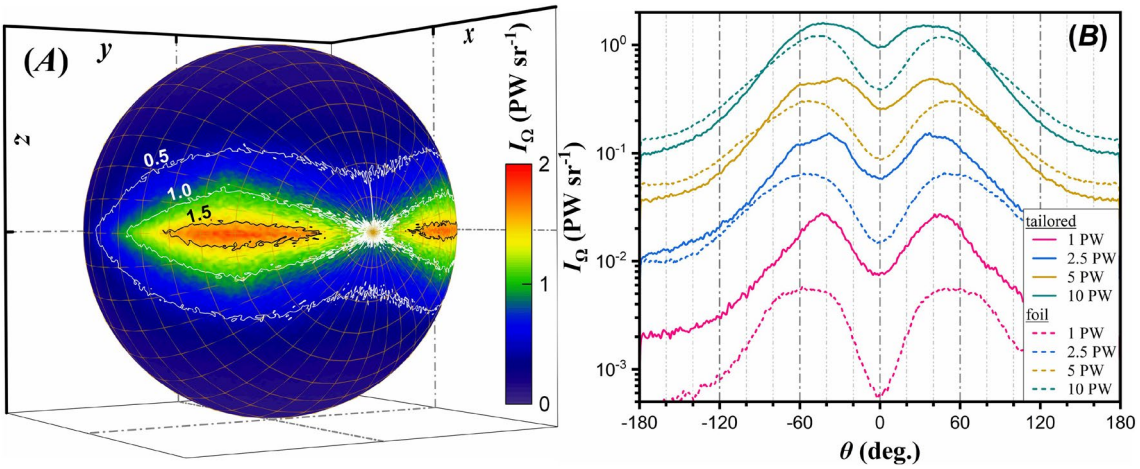

Figure 6. (**A**) Radiant intensity of γ-photons due to the interaction of a 10 PW laser with a tailored lithium target. (**B**) Line-out of the radiant intensity of γ-photons, taken along the polarization plane and within a full-angle divergence of 10^o. The solid lines correspond to tailored lithium targets and the dashed lines to foil targets, for various laser powers as noted in the legend.

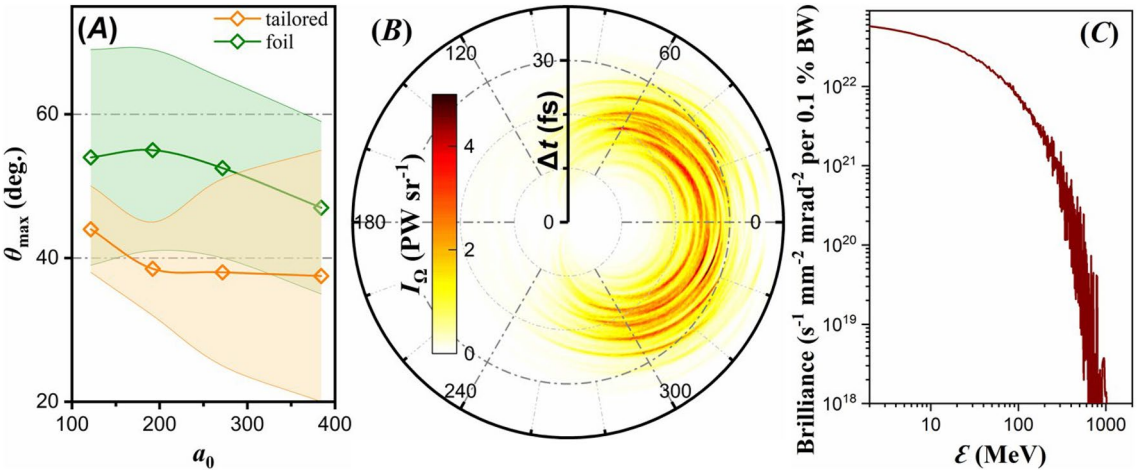

Figure 7. (**A**) Angle of the peak γ-photon radiant intensity as a function of a_0. The tailored and foil target cases are shown by the orange and green lines respectively. The ranges for both cases show the region where the radiant intensity is above 90 % of its peak value. (**B**) Radiant intensity of γ-photons measured within a full-angle divergence of 10^o with respect to the polarization plane, as a function of time-of-flight difference. (**C**) Brilliance for the 10 PW laser case interacting with a lithium tailored target. The corresponding solid angle is at 37.5^o with respect to the laser propagation axis, with a cone full angle of 10^o.

plane, forming a double-lobe pattern. We generalize these results, showing that the double-lobe pattern is a general characteristic of linearly polarized laser-matter interactions, as shown in Fig. 6A. The figure shows the γ-photon radiant intensity, I_Ω (radiant energy per unit time per solid angle), by approximating that the γ-photon emission duration equals to the laser pulse duration.

The double-lobe feature is observed either for tailored or for foil targets, and at all laser power levels. The main difference among the various cases is the γ-ray flash amplitude, as seen in Fig. 6B showing a line-out of the γ-photon radiant intensity, by considering photons emitted within 10^o full-angle with respect to the polarization plane. The peak of Fig. 6A is slightly higher than the peak of Fig. 6B due to the 10^o averaging of the radiant intensity. Our present work aims at providing a scheme that maximises κ_γ for multi-petawatt laser-matter interactions. Although we observe collimation of the resulting γ-ray flashes in two directions, there are other schemes that propose generation of collimated γ-photon beams in a single direction by means of counter-propagating lasers[84], controllable angular momentum[85], wire-targets[86], two-stage acceleration[87] and radially polarised λ^3-lasers[83,88].

Mapping the γ-photon radiant intensity is crucial in experiments aiming on γ-photon production through laser-matter interactions. If one needs to optimise γ-photon detection, the detection system must be aligned along the highest radiant intensity direction[89,90], which in all cases lies on the laser polarization plane. However, the polar angle depends on the laser-matter interaction parameters, where the peak can be seen in Fig. 7A for tailored targets (orange line) and foil targets (green line). The ranges on the plot define where at-least 90 % of the peak

signal is detectable. At all laser power levels, the tailored targets compared to foil targets result in γ-photon peak emission closer to the laser propagation axis, reaching 37^o versus 47^o respectively for a 10 PW laser. Furthermore, in both target cases the peak emission angle moves closer to the laser propagation axis for increased laser power.

The γ-ray flash is usually treated as a time-integrated quantity of a single γ-photon pulse. However, ballistic evolution of the γ-photons allows an angular and temporal discrimination, as shown in Fig. 7B; the temporal axis has an arbitrary (detection distance related) offset, not relevant to revealing the γ-flash dynamics. As seen in the figure, γ-photon emission is directly connected to the laser wavelength in the regions of strongest emission. Temporal discrimination of the γ-ray flash reveals that the localized radiant intensity can reach values as high as 6 PWsr^{-1}. In addition, the γ-photons emitted at symmetric azimuthal angles come with a time difference of half laser period.

The brilliance at a γ-photon energy value $\mathcal{E}_\gamma$ is given by[91]

$$B = \frac{\mathcal{E}_\gamma \left(dN_\gamma / d\mathcal{E}_\gamma\right)}{t_\gamma A \Omega}, \tag{3}$$

where t_γ is the duration of the γ-ray flash, A is the source size, Ω is the corresponding solid angle and the calculation is done for 0.1 % fractional bandwidth, $d\mathcal{E}_\gamma / \mathcal{E}_\gamma$. We record a peak brilliance of 5×10^{22} s^{-1}mm^{-2}mrad^{-2} per 0.1 % bandwidth for the 10 PW laser case interacting with a lithium tailored target as seen in Fig. 7C, being lower than the brilliance from proposed schemes for an extremely collimated γ-photon beam[84]. High brilliance γ-photon sources suit ambitious research programs[92,93] aiming on medicine, industry and nuclear energy applications.

The reduced γ-photon production on the laser propagation axis indicates that the γ-photons do not originate from electrons moving antiparallel to the laser propagation direction, where in that case a peak should had been observed rather than a dip. Instead, the γ-photons are mostly emitted from electrons moving at a non-zero angle along the laser propagation. The lower energy γ-photons that are emitted as an afterglow at later times have an antiparallel direction with respect to the laser propagation axis and are characterized by a larger period. If a circular detector array is centred at the laser focal spot, then the γ-ray flashes will be detected with a time delay, as indicated by the non-centred γ-photon fronts of Fig. 7B, indicating that the major γ-photon emission happens at a shifted position, at a certain depth inside the target cavity.

Conclusions

We present the efficient generation of γ-ray flash through simulations of an ultrashort ultraintense laser interacting with a tailored target, where the target density data are taken from previously published MHD simulation results. The MHD simulations exhibit a unique favourable tailoring of the initially flat target, drilling a conical-like cavity in its volume preceded by an exponentially increasing preplasma distribution. The resulting electron and ion number densities are used as initial conditions for PIC simulations, revealing the effect of the main laser pulse on the tailored target.

The conical-like cavity formation strongly alters the laser interaction compared to the interaction with a foil target. The laser pulse, being of similar temporal extent to the cavity depth is reflected by the cavity walls, increasing the laser field intensity by an order of magnitude. Furthermore, cavity reflection of the laser field allows appearance of a longitudinal electric field component, aiding in further propagation of the cavity. In addition, if a relatively low density solid is chosen as the target material, then the multi-PW laser-target interaction occurs in the relativistically transparent regime, penetrating deep into the target.

The ultrahigh intensities reached are within the regime where nonlinear Compton scattering process dominates the laser-target interaction, being capable of generating a bright γ-ray flash. Although no e^- - e^+ pairs were expected from currently available lasers, we estimate that a significant number of pairs can still be produced due to the multiphoton Breit-Wheeler process by the significant intensity enhancement. It is found that the emitted γ-photons can have an energy approximately equal to the one third of the initial laser energy, with γ-photon energies approaching the GeV-level, if a 10 μm thick tailored lithium foil is used as a target.

The target material is of crucial importance, since a denser material shifts the interaction out of the relativistic transparency regime. In addition, a denser material results in a shallower cavity, that cannot effectively intensify the main laser pulse. As a result, both dense and/or foil targets suppresses the γ-ray yield since the laser field is strongly reflected, which can also pose a higher risk for optical damage of the laser system.

It is found that the γ-photon radiant intensity forms a double-lobe pattern emitted in the polarization plane, which is a general feature of linearly polarized lasers interacting with matter. The γ-photon emission peaks at angles of $37^o - 55^o$ under the parameters examined. In all cases, the emission angle is smaller when the cavity is present in the target.

The temporal dynamics of the γ-ray flash is also revealed, exhibiting direct connection to the laser period. It is found that for azimuthally symmetrical angles the γ-photon emission is temporally shifted by half laser period and is suppressed on the laser propagation axis. This pattern indicates that γ-photon emission originates from electrons co-moving with the laser pulse at a certain angle. Those electrons moving exactly parallel to the pulse produce little-to-no γ-photons, where this behaviour explains the double-lobe pattern observed. In addition, the temporal discrimination of the γ-ray flash reveals radiant intensities significantly higher than previously expected, opening the road to their application in studying astrophysical processes and to effects of photonuclear interactions.

Data Availability

The data that support the findings of this study are available from the corresponding author, PH, upon reasonable request.

Received: 9 May 2022; Accepted: 26 September 2022
Published online: 13 October 2022

References

1. Strickland, D. & Mourou, G. Compression of amplified chirped optical pulses. *Opt. Commun.* **56**, 219–221. https://doi.org/10.1016/0030-4018(85)90120-8 (1985).
2. Danson, C. N. *et al.* Petawatt and exawatt class lasers worldwide. *High Power Laser Sci.* **7**, e54. https://doi.org/10.1017/hpl.2019.36 (2019).
3. Tanaka, K. A. *et al.* Current status and highlights of the ELI-NP research program. *Matter Radiat. at Extremes* **5**, 024402. https://doi.org/10.1063/1.5093535 (2020).
4. Osvay, K. *et al.* Development status and operation experiences of the few cycle high average power lasers of ELI-ALPS (Conference Presentation). In Bakule, P. & Haefner, C. L. (eds.) *Short-pulse High-energy Lasers and Ultrafast Optical Technologies*, vol. 11034, https://doi.org/10.1117/12.2523057.International Society for Optics and Photonics (SPIE, 2019).
5. Papadopoulos, D. *et al.* The Apollon 10 PW laser: Experimental and theoretical investigation of the temporal characteristics. *High Power Laser Sci. Eng.* **4**, e34. https://doi.org/10.1017/hpl.2016.34 (2016).
6. Kiriyama, H. *et al.* High-contrast high-intensity repetitive petawatt laser. *Opt. Lett.* **43**, 2595–2598. https://doi.org/10.1364/OL.43.002595 (2018).
7. Yoon, J. W. *et al.* Realization of laser intensity over $10^{23}\,W/cm^2$. *Optica* **8**, 630–635, https://doi.org/10.1364/OPTICA.420520(2021).
8. Mourou, G. A., Tajima, T. & Bulanov, S. V. Optics in the relativistic regime. *Rev. Mod. Phys.* **78**, 309–371. https://doi.org/10.1103/RevModPhys.78.309 (2006).
9. Dubietis, A., Jonušauskas, G. & Piskarskas, A. Powerful femtosecond pulse generation by chirped and stretched pulse parametric amplification in BBO crystal. *Opt. Commun.* **88**, 437–440. https://doi.org/10.1016/0030-4018(92)90070-8 (1992).
10. Lévy, A. *et al.* Double plasma mirror for ultrahigh temporal contrast ultraintense laser pulses. *Opt. Lett.* **32**, 310–312. https://doi.org/10.1364/OL.32.000310 (2007).
11. Giulietti, D. *et al.* Production of ultracollimated bunches of multi-MeV electrons by 35 fs laser pulses propagating in exploding-foil plasmas. *Phys. Plasmas* **9**, 3655–3658. https://doi.org/10.1063/1.1498116 (2002).
12. Matsukado, K. *et al.* Energetic Protons from a few-micron metallic foil evaporated by an intense laser pulse. *Phys. Rev. Lett.* **91**, 215001. https://doi.org/10.1103/PhysRevLett.91.215001 (2003).
13. Yogo, A. *et al.* Laser ion acceleration via control of the near-critical density target. *Phys. Rev. E* **77**, 016401. https://doi.org/10.1103/PhysRevE.77.016401 (2008).
14. Ogura, K. *et al.* Proton acceleration to 40 MeV using a high intensity, high contrast optical parametric chirped-pulse amplification/Ti:sapphire hybrid laser system. *Opt. Lett.* **37**, 2868–2870. https://doi.org/10.1364/OL.37.002868 (2012).
15. Utsumi, T., Matsukado, K., Daido, H., Esirkepov, T. & Bulanov, S. Numerical simulation of melting and evaporation of a cold foil target irradiated by a pre-pulse. *Appl. Phys. A* **79**, 1185–1187. https://doi.org/10.1007/s00339-004-2700-4 (2004).
16. Esirkepov, T. Z. *et al.* Prepulse and amplified spontaneous emission effects on the interaction of a petawatt class laser with thin solid targets. *Nucl. Instr. Meth. Phys. Res. A* **745**, 150–163. https://doi.org/10.1016/j.nima.2014.01.056 (2014).
17. Hadjisolomou, P. *et al.* Preplasma effects on laser ion generation from thin foil targets. *Phys. Plasmas* **27**, 013107 (2020).
18. Schwoerer, H. *et al.* Laser-plasma acceleration of quasi-monoenergetic protons from microstructured targets. *Nature* **439**, 445–448. https://doi.org/10.1038/nature04492 (2006).
19. Toncian, T. *et al.* Ultrafast laser-driven microlens to focus and energy-select mega-electron volt protons. *Science* **312**, 410–413. https://doi.org/10.1126/science.1124412 (2006).
20. Kar, S. *et al.* Dynamic control of laser-produced proton beams. *Phys. Rev. Lett.* **100**, 105004. https://doi.org/10.1103/PhysRevLett.100.105004 (2008).
21. Burza, M. *et al.* Hollow microspheres as targets for staged laser-driven proton acceleration. *New J. Phys.* **13**, 013030. https://doi.org/10.1088/1367-2630/13/1/013030 (2011).
22. Kar, S. *et al.* Guided post-acceleration of laser-driven ions by a miniature modular structure. *Nat. Commun.* **7**, 10792. https://doi.org/10.1038/ncomms10792 (2016).
23. Psikal, J., Grym, J., Stolcova, L. & Proska, J. Hollow target for efficient generation of fast ions by ultrashort laser pulses. *Phys. Plasmas* **23**, 123121. https://doi.org/10.1063/1.4972880 (2016).
24. Hadjisolomou, P., Bulanov, S. V. & Korn, G. Towards laser ion acceleration with holed targets. *J. Plasma Phys.* **86**, 905860304. https://doi.org/10.1017/S0022377820000379 (2020).
25. Gitomer, S. J. *et al.* Fast ions and hot electrons in the laser-plasma interaction. *Phys. Fluids* **29**, 2679–2688. https://doi.org/10.1063/1.865510 (1986).
26. Dorrer, C. & Spilatro, M. Spectral and temporal shaping of spectrally incoherent pulses in the infrared and ultraviolet. *Opt. Exp.* **30**, 4942–4953. https://doi.org/10.1364/OE.449418 (2022).
27. Borghesi, M. *et al.* Characterization of laser plasmas for interaction studies: Progress in time-resolved density mapping. *Phys. Rev. E* **54**, 6769–6773. https://doi.org/10.1103/PhysRevE.54.6769 (1996).
28. Gizzi, L. A. *et al.* Enhanced laser-driven proton acceleration via improved fast electron heating in a controlled pre-plasma. *Sci. Rep.* **11**, 13728. https://doi.org/10.1038/s41598-021-93011-3 (2021).
29. Gonsalves, A. J. *et al.* Petawatt laser guiding and electron beam acceleration to 8 GeV in a laser-heated capillary discharge waveguide. *Phys. Rev. Lett.* **122**, 084801. https://doi.org/10.1103/PhysRevLett.122.084801 (2019).
30. Nakamura, T. *et al.* High-power γ-Ray flash generation in ultraintense laser-plasma interactions. *Phys. Rev. Lett.* **108**, 195001. https://doi.org/10.1103/PhysRevLett.108.195001 (2012).
31. Ridgers, C. P. *et al.* Dense electron-positron plasmas and bursts of gamma-rays from laser-generated quantum electrodynamic plasmas. *Phys. Plasmas* **20**, 056701. https://doi.org/10.1063/1.4801513 (2013).
32. Lezhnin, K. V., Sasorov, P. V., Korn, G. & Bulanov, S. V. High power gamma flare generation in multi-petawatt laser interaction with tailored targets. *Phys. Plasmas* **25**, 123105. https://doi.org/10.1063/1.5062849 (2018).
33. Younis, A. H., Davidson, A., Hafizi, B. & Gordon, D. F. Diagnostic Techniques for particle-in-cell simulations of laser-produced gamma-rays in the strong-field QED regime. **2106**, 16227 (2021).
34. Koch, H. W. & Motz, J. W. Bremsstrahlung cross-section formulas and related data. *Rev. Mod. Phys.* **31**, 920–955. https://doi.org/10.1103/RevModPhys.31.920 (1959).
35. Vyskočil, J., Klimo, O. & Weber, S. Simulations of bremsstrahlung emission in ultra-intense laser interactions with foil targets. *Plasma Phys. Control. Fusion* **60**, 054013. https://doi.org/10.1088/1361-6587/aab4c3 (2018).
36. Radier, C. *et al.* 10 PW peak power femtosecond laser pulses at ELI-NP. *High Power Laser Sci. Eng.* **10**, e21. https://doi.org/10.1017/hpl.2022.11 (2022).
37. Rinderknecht, H. G. *et al.* Relativistically transparent magnetic filaments: scaling laws, initial results and prospects for strong-field QED studies. *New J. Phys.* **23**, 095009. https://doi.org/10.1088/1367-2630/ac22e7 (2021).
38. Ehlotzky, F., Krajewska, K. & Kamiński, J. Z. Fundamental processes of quantum electrodynamics in laser fields of relativistic power. *Rep. Prog. Phys.* **72**, 046401. https://doi.org/10.1088/0034-4885/72/4/046401 (2009).

39. Ledingham, K. W. D. *et al.* Photonuclear physics when a multiterawatt laser pulse interacts with solid targets. *Phys. Rev. Lett.* **84**, 899–902. https://doi.org/10.1103/PhysRevLett.84.899 (2000).
40. Nedorezov, V. G., Turinge, A. A., & Shatunov, Y. M. Photonuclear experiments with Compton-backscattered gamma beams. *Phys.-Uspekhi***47**, 341–358, https://doi.org/10.1070/pu2004v047n04abeh001743(2004).
41. Eliasson, B. & Liu, C. S. An electromagnetic gamma-ray free electron laser. *J. Plasma Phys.* **79**, 995–998. https://doi.org/10.1017/S0022377813000779 (2013).
42. Rees, M. J. & Mészáros, P. Relativistic fireballs: Energy conversion and time-scales. *Mon. Not. R. Astron. Soc.* **258**, 41P-43P. https://doi.org/10.1093/mnras/258.1.41P (1992).
43. Bulanov, S. V. *et al.* On the problems of relativistic laboratory astrophysics and fundamental physics with super powerful lasers. *Plasma Phys. Rep.* **41**, 1–51. https://doi.org/10.1134/S1063780X15010018 (2015).
44. Philippov, A. A. & Spitkovsky, A. Ab-initio pulsar magnetosphere: Particle acceleration in oblique rotators and high-energy emission modeling. *Astrophys. J.* **855**, 94. https://doi.org/10.3847/1538-4357/aaabbc (2018).
45. Aharonian, F. *et al.* Extended very-high-energy gamma-ray emission surrounding PSR J 0622+3749 observed by LHAASO-KM2A. *Phys. Rev. Lett.***126**, 241103. https://doi.org/10.1103/PhysRevLett.126.241103 (2021).
46. Zhidkov, A., Koga, J., Sasaki, A. & Uesaka, M. Radiation damping effects on the interaction of ultraintense laser pulses with an overdense plasma. *Phys. Rev. Lett.* **88**, 185002. https://doi.org/10.1103/PhysRevLett.88.185002 (2002).
47. Koga, J., Esirkepov, T. Z. & Bulanov, S. V. Nonlinear Thomson scattering in the strong radiation damping regime. *Phys. Plasmas* **12**, 093106. https://doi.org/10.1063/1.2013067 (2005).
48. Gu, Y. J., Klimo, O., Bulanov, S. V. & Weber, S. Brilliant gamma-ray beam and electron-positron pair production by enhanced attosecond pulses. *Commun. Phys.* **1**, 1–9. https://doi.org/10.1038/s42005-018-0095-3 (2018).
49. Bell, A. R. & Kirk, J. G. Possibility of prolific pair production with high-power lasers. *Phys. Rev. Lett.* **101**, 200403. https://doi.org/10.1103/PhysRevLett.101.200403 (2008).
50. Kirk, J. G., Bell, A. R. & Arka, I. Pair production in counter-propagating laser beams. *Plasma Phys. Control. Fusion* **51**, 085008. https://doi.org/10.1088/0741-3335/51/8/085008 (2009).
51. Luo, W. *et al.* Dense electron-positron plasmas and gamma-ray bursts generation by counter-propagating quantum electrodynamics-strong laser interaction with solid targets. *Phys. Plasmas* **22**, 063112. https://doi.org/10.1063/1.4923265 (2015).
52. Grismayer, T., Vranic, M., Martins, J. L., Fonseca, R. A. & Silva, L. O. Laser absorption via quantum electrodynamics cascades in counter propagating laser pulses. *Phys. Plasmas* **23**, 056706. https://doi.org/10.1063/1.4950841 (2016).
53. Vranic, M., Grismayer, T., Fonseca, R. A. & Silva, L. O. Electron-positron cascades in multiple-laser optical traps. *Plasma Phys. Control. Fusion* **59**, 014040. https://doi.org/10.1088/0741-3335/59/1/014040 (2016).
54. Gong, Z. *et al.* High-efficiency γ-ray flash generation via multiple-laser scattering in ponderomotive potential well. *Phys. Rev. E* **95**, 013210. https://doi.org/10.1103/PhysRevE.95.013210 (2017).
55. Ji, L. L., Snyder, J. & Shen, B. F. Single-pulse laser-electron collision within a micro-channel plasma target. *Plasma Phys. Control. Fusion* **61**, 065019. https://doi.org/10.1088/1361-6587/ab1692 (2019).
56. Zhang, L. Q. *et al.* Brilliant attosecond γ-ray emission and high-yield positron production from intense laser-irradiated nano-micro array. *Phys. Plasmas* **28**, 023110. https://doi.org/10.1063/5.0030909 (2021).
57. Sarri, G. *et al.* Ultrahigh brilliance multi-MeV γ-ray beams from nonlinear relativistic Thomson scattering. *Phys. Rev. Lett.* **113**, 224801. https://doi.org/10.1103/PhysRevLett.113.224801 (2014).
58. Magnusson, J. *et al.* Laser-particle collider for multi-Gev photon production. *Phys. Rev. Lett.* **122**, 254801. https://doi.org/10.1103/PhysRevLett.122.254801 (2019).
59. Wang, X. B. *et al.* Gamma-ray generation from ultraintense laser-irradiated solid targets with preplasma. *High Power Laser Sci. Eng.* **8**, e34. https://doi.org/10.1017/hpl.2020.30 (2020).
60. Tsygvintsev, I. P. Results of RHD simulation of ns-prepulse with 3DLINE code for different target materials, https://doi.org/10.5281/ZENODO.6412637(2022). Data come under CC BY 4.0 license.
61. Arber, T. D. *et al.* Contemporary particle-in-cell approach to laser-plasma modelling. *Plasma Phys. Control. Fusion* **57**, 113001. https://doi.org/10.1088/0741-3335/57/11/113001 (2015).
62. Higuera, A. V. & Cary, J. R. Structure-preserving second-order integration of relativistic charged particle trajectories in electromagnetic fields. *Phys. Plasmas* **24**, 052104 (2017).
63. Ridgers, C. P. *et al.* Modelling gamma-ray photon emission and pair production in high-intensity laser-matter interactions. *J. Comput. Phys.* **260**, 273–285. https://doi.org/10.1016/j.jcp.2013.12.007 (2014).
64. Kodama, R. *et al.* Fast heating scalable to laser fusion ignition. *Nature* **418**, 933–934. https://doi.org/10.1038/418933a (2002).
65. Kamboj, O., Ghotra, H. S., Thakur, V., Pasley, J. & Kant, N. Optimizing laser focal spot size using self-focusing in a cone-guided fast-ignition ICF target. *Eur. Phys. J. Plus* **136**, 484. https://doi.org/10.1140/epjp/s13360-021-01488-8 (2021).
66. Chintalwad, S., Krishnamurthy, S., Ramakrishna, B. & Ridgers, C. P. Photon emission enhancement studies from the interaction of ultraintense laser pulses with shaped targets. *Phys. Rev. E* **105**, 025205. https://doi.org/10.1103/PhysRevE.105.025205 (2022).
67. Budriga, O., Ionel, L. E., Tatomirescu, D. & Tanaka, K. A. Enhancement of laser-focused intensity greater than 10 times through a re-entrant cone in the petawatt regime. *Opt. Lett.* **45**, 3454–3457. https://doi.org/10.1364/OL.395316 (2020).
68. Badziak, J. *et al.* Highly efficient accelerator of dense matter using laser-induced cavity pressure acceleration. *Phys. Plasmas* **19**, 053105. https://doi.org/10.1063/1.4714660 (2012).
69. Busold, S. *et al.* Focusing and transport of high-intensity multi-MeV proton bunches from a compact laser-driven source. *Phys. Rev. ST Accel. Beams* **16**, 101302. https://doi.org/10.1103/PhysRevSTAB.16.101302 (2013).
70. Naumova, N. *et al.* Hole boring in a DT pellet and fast-ion ignition with ultraintense laser pulses. *Phys. Rev. Lett.* **102**, 025002. https://doi.org/10.1103/PhysRevLett.102.025002 (2009).
71. Schlegel, T. *et al.* Relativistic laser piston model: Ponderomotive ion acceleration in dense plasmas using ultraintense laser pulses. *Phys. Plasmas* **16**, 083103. https://doi.org/10.1063/1.3196845 (2009).
72. Wilks, S. C., Kruer, W. L., Tabak, M. & Langdon, A. B. Absorption of ultra-intense laser pulses. *Phys. Rev. Lett.* **69**, 1383–1386. https://doi.org/10.1103/PhysRevLett.69.1383 (1992).
73. Pukhov, A., Sheng, Z. M. & Meyer-ter Vehn, J. Particle acceleration in relativistic laser channels. *Phys. Plasmas* **6**, 2847–2854. https://doi.org/10.1063/1.873242 (1999).
74. Feit, M. D., Komashko, A. M. & Rubenchik, A. M. Relativistic self-focusing in underdense plasma. *Phys. D: Nonlinear Phenom.* **152–153**, 705–713. https://doi.org/10.1016/S0167-2789(01)00203-2 (2001).
75. Mangles, S. P. D. *et al.* Electron acceleration in cavitated channels formed by a petawatt laser in low-density plasma. *Phys. Rev. Lett.* **94**, 245001. https://doi.org/10.1103/PhysRevLett.94.245001 (2005).
76. von Seggern, D. H. *CRC Standard Curves and Surfaces with Mathematica* (Chapman and Hall / CRC, 2016).
77. Vshivkov, V. A., Naumova, N. M., Pegoraro, F. & Bulanov, S. V. Nonlinear electrodynamics of the interaction of ultra-intense laser pulses with a thin foil. *Phys. Plasmas* **5**, 2727–2741. https://doi.org/10.1063/1.872961 (1998).
78. Esirkepov, T., Yamagiwa, M. & Tajima, T. Laser ion-acceleration scaling laws seen in multiparametric particle-in-cell simulations. *Phys. Rev. Lett.* **96**, 105001. https://doi.org/10.1103/PhysRevLett.96.105001 (2006).
79. Esberg, J. *et al.* Experimental investigation of strong field trident production, collaboration=CERN NA63. *Phys. Rev. D* **82**, 072002. https://doi.org/10.1103/PhysRevD.82.072002 (2010).

80. Chen, H. *et al.* Relativistic Quasimonoenergetic positron jets from intense laser-solid interactions. *Phys. Rev. Lett.* **105**, 015003. https://doi.org/10.1103/PhysRevLett.105.015003 (2010).
81. Stark, D. J., Toncian, T. & Arefiev, A. V. Enhanced multi-mev photon emission by a laser-driven electron beam in a self-generated magnetic field. *Phys. Rev. Lett.* **116**, 185003. https://doi.org/10.1103/PhysRevLett.116.185003 (2016).
82. Wang, T. *et al.* Power scaling for collimated γ-ray beams generated by structured laser-irradiated targets and its application to two-photon pair production. *Phys. Rev. Appl.* **13**, 054024. https://doi.org/10.1103/PhysRevApplied.13.054024 (2020).
83. Hadjisolomou, P. *et al.* Gamma-ray flash in the interaction of a tightly focused single-cycle ultra-intense laser pulse with a solid target. *J. Plasma Phys.* **88**, 905880104. https://doi.org/10.1017/S0022377821001318 (2022).
84. Zhu, X. L. *et al.* Dense GeV electron-positron pairs generated by lasers in near-critical-density plasmas. *Nat. Commun.* **7**, 13686. https://doi.org/10.1038/ncomms13686 (2016).
85. Zhu, X. L., Yu, T. P., Chen, M., Weng, S. M. & Sheng, Z. M. Generation of GeV positron and γ-photon beams with controllable angular momentum by intense lasers. *New J. Phys.* **20**, 083013. https://doi.org/10.1088/1367-2630/aad71a (2018).
86. Wang, W. M. *et al.* Collimated ultrabright gamma rays from electron wiggling along a petawatt laser-irradiated wire in the QED regime. *Proc. Natl. Acad. Sci.* **115**, 9911–9916. https://doi.org/10.1073/pnas.1809649115 (2018).
87. Zhu, X. L. *et al.* Extremely brilliant GeV γ-rays from a two-stage laser-plasma accelerator. *Sci. Adv.* **6**, eaaz7240. https://doi.org/10.1126/sciadv.aaz7240 (2020).
88. Hadjisolomou, P., Jeong, T. M., Valenta, P., Korn, G. & Bulanov, S. V. Gamma-ray flash generation in irradiating a thin foil target by a single-cycle tightly focused extreme power laser pulse. *Phys. Rev. E* **104**, 015203. https://doi.org/10.1103/PhysRevE.104.015203 (2021).
89. Singh, S. *et al.* Compact high energy x-ray spectrometer based on forward compton scattering for high intensity laser plasma experiments. *Rev. Sci. Instrum.* **89**, 085118. https://doi.org/10.1063/1.5040979 (2018).
90. Singh, S. *et al.* Bremsstrahlung emission and plasma characterization driven by moderately relativistic laser-plasma interactions. *Plasma Phys. Control. Fusion* **63**, 035004. https://doi.org/10.1088/1361-6587/abcf7e (2021).
91. Hertel, I. V. & Schulz, C. P. *Atoms (Molecules and Optical Physics Atomic Physics and Basics of Spectroscopy* (Springer, Berlin, 2008).
92. Gales, S. *et al.* New frontiers in nuclear physics with high-power lasers and brilliant monochromatic gamma beams. *Phys. Scr.* **91**, 093004. https://doi.org/10.1088/0031-8949/91/9/093004 (2016).
93. Gales, S. *et al.* The extreme light infrastructure-nuclear physics (ELI-NP) facility: new horizons in physics with 10 PW ultra-intense lasers and 20 MeV brilliant gamma beams. *Rep. Prog. Phys.* **81**, 094301. https://doi.org/10.1088/1361-6633/aacfe8 (2018).

Acknowledgements

The authors would like to thank Ilia P. Tsygvintsev and Vladimir A. Gasilov for providing the MHD simulation results[60] and for fruitful discussions. The authors also acknowledge useful communication with Pavel Sasorov on MHD simulations and Martin Matys on computational aspects. This work is supported by the projects High Field Initiative (CZ.02.1.01/0.0/0.0/15_003/0000449) from the European Regional Development Fund. The EPOCH code is in part funded by the UK EPSRC grants EP/G054950/1, EP/G056803/1, EP/G055165/1 and EP/M022463/1.

Author contributions

Author contributions: P.H., T.M.J. and S.V.B. conceived the work and participated in the interpretation of results; P.H. performed the PIC simulations and analysed the data.

Competing interests

The authors declare no competing interests.

Additional information

Correspondence and requests for materials should be addressed to P.H.